Title

Combined magnetic resonance imaging and optical surgical navigation system guidance of percutaneous liver cryoablation in a porcine model.

Journal

American Journal of Translational Research, 10(5)

ISSN

1943-8141

Authors

Zhou, Kang
Zhang, Zhuoli
Figini, Matteo
et al.

Publication Date

2018

Am J Transl Res 2018;10(5):1531-1538
www.ajtr.org /ISSN:1943-8141/AJTR0069150

Original Article

Combined magnetic resonance imaging and optical surgical navigation system guidance of percutaneous liver cryoablation in a porcine model

Kang Zhou[1], Zhuoli Zhang[2], Matteo Figini[2], Junjie Shangguan[2], Yining Wang[1], Haifeng Shi[1], Yumei Li[1], Zhengyu Jin[1*], Jie Pan[1*]

[1]Department of Radiology, Peking Union Medical College Hosptial, Chinese Academy of Medical Sciences, Shuaifuyuan 1#, Dongcheng District, Beijing 100730, China; [2]Department of Radiology, Northwestern University, Chicago, IL 60611, United States. [*]Equal contributors.

Received November 14, 2017; Accepted April 13, 2018; Epub May 15, 2018; Published May 30, 2018

Abstract: The efficacy and safety of combining open-configuration magnetic resonance imaging (MRI) and an optical surgical navigation system (OSNS) for guidance of percutaneous liver cryoablation were evaluated in a pig model. This approach was successfully executed in eight test pigs under general anesthesia. Another two pigs spared from ablation served as controls. MRI studies, blood testing, and pathologic examinations were performed at various time points. MRI-determined minimal and maximal cryolesion diameters were 19.4 ± 1.5 mm and 44.3 ± 1.8 mm, respectively (mean volume, 8.32 ± 2.41 cm^3). The lesions were readily visible by MRI on postablation Days 2 and 7, all presenting as teardrop-shaped regions of low signal intensity in T1-weighted images and high signal intensity in T2-weighted images. Mean serum alanine aminotransferase concentration transiently increased postablation, and mean blood platelet count transiently declined (both, $P < 0.05$). The mean necrotic tissue volume generated by pathologic assessment was less than that determined by MRI (4.24 ± 2.3 cm^3 vs. 8.32 ± 2.41 cm^3, $P < 0.05$). Cell necrosis isotherms in MRI views were within 6.0 ± 0.8 mm of cryolesion edges. Inflammatory cell infiltrates and exuberant granulation tissue surrounded necrotic areas on postablation Day 7. Combined open-configuration MRI and OSNS guidance of percutaneous liver cryoablation proved effective and safe in our animal model. This concept seems ideal for precision image-guided hepatic ablation in a clinical setting.

Keywords: Cryoablation, pig model, liver model, magnetic resonance imaging, optical surgical navigation system, image-guided

Introduction

Hepatocellular carcinoma (HCC) is the third most common cause of cancer-related deaths [1, 2], and tumor metastasis to liver is more common still than primary liver cancer [3]. Although surgical resection or transplantation offers a potential for cure, only 10-15% of patients qualify for such procedures [2-5].

If surgical intervention is prohibitive, image-guided tumor ablation is the preferred therapeutic option [6]. This approach includes two broad strategies: 1) chemical ablation, such as percutaneous ethanol instillation, and 2) thermal ablation through radiofrequency (RF) exposure, microwave coagulation, or cryoablative techniques. These are effective low-risk treatment modalities for targeted local control of liver tumors [6-10]. Although RF ablation has been more widely used, the advantages of cryoablation include excellent visibility of ablation zones by computed tomography (CT) or magnetic resonance imaging (MRI) [11]; adjustability of cryogen gas rate to control size and shape of ablation effect; and far less procedure-related pain compared with other ablative techniques, allowing delivery of local anesthesia only for most cryoablation procedures [12-14].

Early cryoablation systems encumbered by large probes (diameters beyond 11-G) carried

risks of hepatic fissures and severe hemorrhage [15]. Ultrasonography (US) is typically engaged to monitor ice ball formation during cryoablation. However, signal reflection from the interface of frozen and non-frozen tissue impedes single-view whole-lesion assessment [16]. MRI overcomes this drawback, ensuring visualization of the entire ice ball [17, 18]. The smaller MR-compatible cryoprobes (diameters under 13-G) permit percutaneous entry, and the open-configuration MRI systems now available facilitate needle-probe placement and intraprocedural treatment monitoring. A novel optical surgical navigation system (OSNS) recently introduced is equipped with near-infrared cameras for tracking probe position in real-time. This system creates an adjustable linear graphic line that is merged with MRI views for preoperative lesion localization, entry-point skin marking, procedural planning, and intraoperative guidance [19, 20].

In this study, we successfully performed percutaneous MRI and OSNS-guided hepatic cryoablation in pigs under general anesthesia. Follow-up MRI studies, blood testing, and pathologic examinations were also undertaken at various time points. Our aim was to evaluate the feasibility and benefits of this approach in a porcine model. Present findings suggest that combined open-configuration MRI and OSNS guidance of percutaneous liver cryoablation is effective and safe in this animal model and may be ideal for precision image-guided hepatic ablation in a clinical setting.

Materials and methods

Animals, anesthesia, and procedures

All studies were approved by our institutional Animal Care and Use Committee and were performed in accordance with National Institute of Health (NIH) guidelines. Ten healthy male minipigs (mean weight, 21.2 kg ± 3.4 kg; Animal Experimental Center of Peking Union Medical College, Beijing, China) were selected for study, using ketamine (intramuscular, 20 mg/kg) and sodium thiopental (intravenous, 5-8 mg/kg, Sodium Pentothol; Abbott Laboratories, Chicago, IL, USA) to induce anesthesia. Isoflurane (1.5%) and oxygen (3 L/min) were administered by mask for maintenance. Eight test pigs (group 1) were subjected to single-probe cryoablation, sparing the remaining two (group 2) to serve as controls.

Cryoablation with MRI and OSNS guidance

Cryoablation procedures were monitored by open-configuration MRI system (Centauri 0.3T; XinAoMDT Technology, Langfang, Hebei, China) as an integral OSNS (XinAoMDT) component. The OSNS included an outer-room console, an in-room monitor, two infrared cameras, a static magnetic body tracker with reflective spheres, and a probe holder with reflective spheres. Using the reflective spheres, optical tracking was achieved through infrared cameras, mapping the probe-holder position in real-time by charting its position in space relative to the fixed magnetic body tracker.

Each pig was placed in left lateral decubitus position after anesthesia. At baseline (pre-cryoablation), three perpendicular images were generated via T1-weighted scan (FOV, 300 × 300; TR/TE, 200-500/20; slice thickness/slice interval, 6.0 mm/2.0 mm; matrix, 192 × 192). An adjustable real-time linear graphic of OSNS creation was then superimposed upon these three images, all shown on an in-room monitor. Preliminary localization, entry-point skin marking, procedural planning, and intraoperative guidance were thereby achieved. A 2D fast spin echo sequence (FOV, 250 × 250; TR/TE, 200-500/20; slice thickness/slice interval, 8.0 mm/2.0 mm; matrix, 192 × 192) was used to scan animals during freezing procedures.

Percutaneous cryotherapy was undertaken using a MRI-compatible cryotherapy delivery system (Cryo-Hit; Galil Medical Ltd, Yokneam, Israel). This argon-helium cryoablation system is based on Joule-Thomson effect [6]. Rapid expansion of pressured argon gas within the probe lowers the temperature at its tip to an extremely low level (-185°C), thus producing an ice ball. High-pressure helium is similarly insufflated (same system), warming the cryoprobe upon atmospheric pressure release to thaw the ice ball.

Through combined MRI/OSNS guidance as described, a 17-G MRI-compatible cryoprobe was inserted into targeted sites of right hepatic lobe. The argon gas (for freezing) was pressurized to 3500 psi, and helium (for thawing) was pressurized to 2200 psi. Two freeze (15

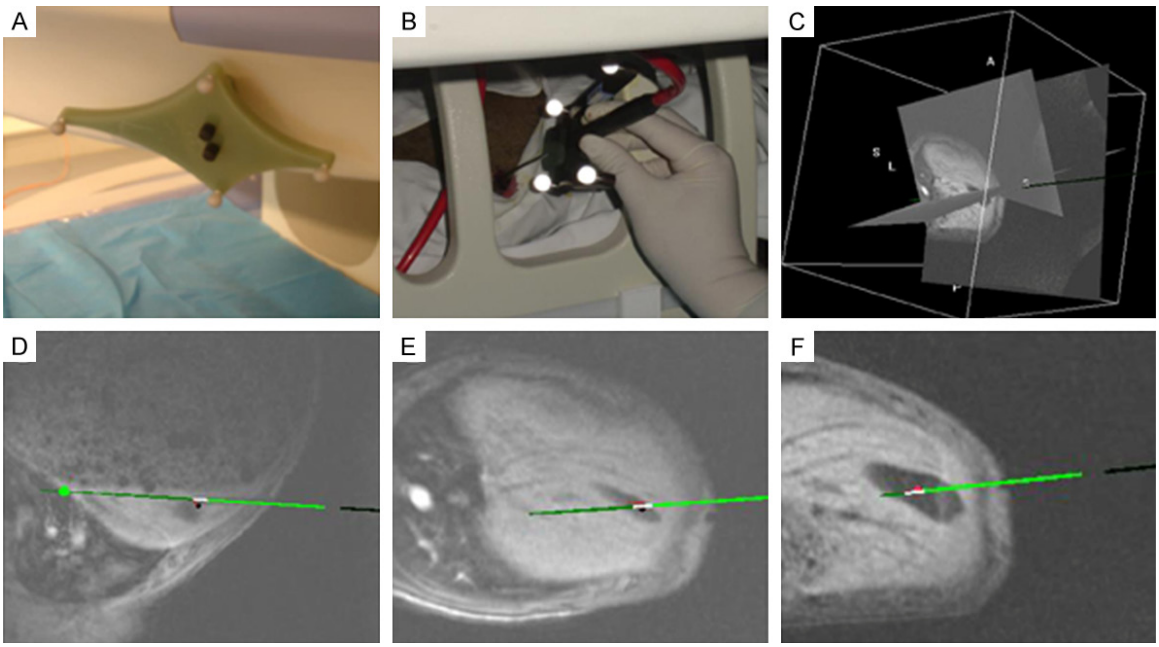

Figure 1. MRI and OSNS-guided needle insertion: A: Fixed magnetic body trackers with reflective spheres; B: Use of needle holder with four reflective spheres during MRI-guided procedure; C-F: Navigation line overlay (green line) in multi-planar MR images, indicating planned trajectory for needle guidance. MRI, magnetic resonance imaging; OSNS, optical surgical navigation system.

min)-thaw (10 min) cycles were completed. Intramuscular buprenorphine (0.9 mg; Reckitt Benckiser Pharmaceuticals, Richmond, VA, USA) injection served to control postprocedural pain.

Follow-up MRI evaluation

In animals of group 1, follow-up MRI studies entailed use of the same scanner at different time points (postablation Days 2, 7, 15, and 30). Conventional 2D fast spin-echo T1-weighted (T1W) images (FOV, 300 × 300; TR/TE, 200-500/20; slice thickness/slice interval, 6.0 mm/1.0 mm; matrix, 256 × 256) and 2D fast spin-echo T2-weighted (T2W) images (FOV, 300 × 300; TR/TE, 4000/90; slice thickness/slice interval, 6.0 mm/1.0 mm; matrix, 256 × 256) were obtained in transverse plane for separate review by two radiologists (5 and 10 years of experience). Advantage Windows v2.0 basic display software (General Electric Company, Milwaukee, WI, USA) enabled MRI analysis. Minimal and maximal ice ball diameters were calculated. Volumes were also estimated as sums of cryolesion areas from each slice multiplied by slice thickness (incorporating gap to adjacent slice).

Blood testing

Blood samples were routinely collected from ear veins of pigs (both groups) under anesthesia, obtaining samples at baseline and sequentially after cryoablation (Days 2, 4, 7, 10, 15, 20, and 30). The specimens were processed at the central laboratory of our hospital. Serum alanine aminotransferase (ALT), bilirubin, alkaline phosphatase (ALKP), myoglobin, and creatinine levels, as well as platelet (PLT) count, white blood cell (WBC) count, and hematocrit values, were recorded.

Pathologic assessment

Animals of group 1 were euthanized in pairs at intervals (immediately after cryoablation and on postablation Days 7, 15, and 30) by sodium pentobarbital overdose. The two control pigs of group 2 were euthanized after blood samples were collected on Day 30. Each liver was removed, fixed in formalin, and later grossly inspected, measuring diameters of cryolesions by ruler. Sections of cryolesions and surrounding tissues were routinely processed for paraffin embedding. The site of cryoprobe insertion served as central axis of dissection. Paraffiniz-

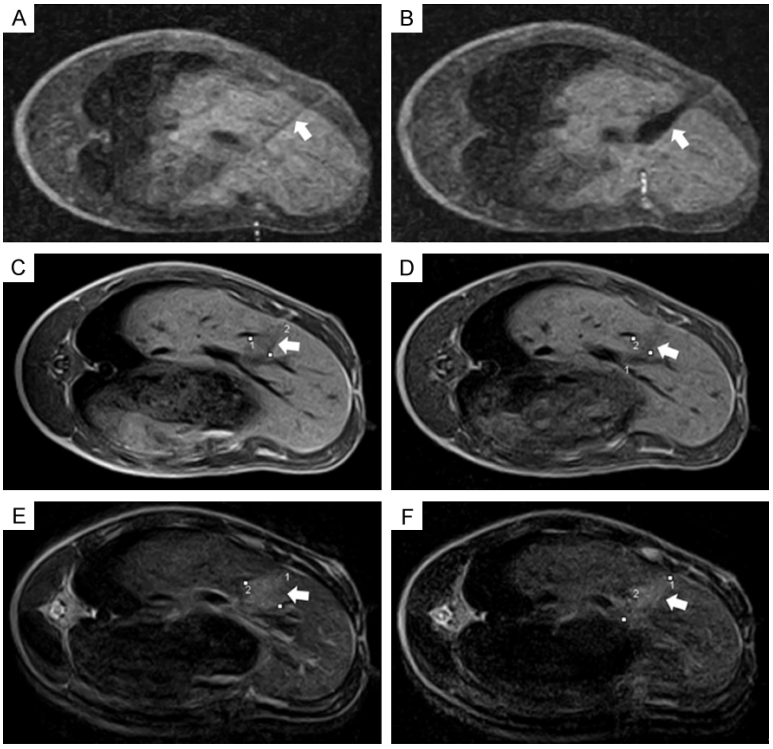

Figure 2. Intraoperative and follow-up MRI views: A, B: Intraoperative scanning images showing needle (arrow) inserted in right hepatic lobe and ice ball under formation (arrow); C, D: T1-weighted images acquired 2 days and 7 days postablation. Cryolesion (arrows) presents as teardrop-shaped region of low signal intensity; E, F: Cryoablated area (arrows) presents as high signal intensity on T2-weighted images acquired 2 days and 7 days after procedure. Lines drawn on images indicate minimal and maximal diameters of cryolesions. MRI, magnetic resonance imaging.

ed samples were serially sectioned (4 μm) for slide preparation, subsequent hematoxylin and eosin (H&E) staining, and examination by pathologists. Histologic zones of coagulative necrosis were mapped using a calibrated microscope. Sizes of lesions were analyzed using Java-based image-handling software developed by the NIH (ImageJ freeware; available at: https://imagej.nih.gov/ij/download.html). The area of each lesion was multiplied by slice thickness, summing volumes of all slices to obtain total volume.

Statistical analysis

SPSS (SPSS v18; IBM, Armonk, NY, USA) was engaged for all statistical computations. Quantitative data were expressed as mean ± standard deviation. Univariate ANOVA was applied to assess between-group differences in blood test data. Cryolesion volumes, as determined by MRI and pathologic examination, were subject to comparison using paired Student's *t*-test. Statistical significance was set at $P < 0.05$.

Results

Postprocedural animal status

All animals survived and fully completed the cryoablation protocol without apparent complications. In fact, all resumed normal eating, defecation, and urination upon recovery from anesthesia. No intraperitoneal hemorrhage, sepsis, or fissuring of liver surface was detected during postmortem abdominal exploration.

MRI and OSNS guidance

Under the guidance of MRI imaging and OSNS, all cryoprobes were successfully inserted into targeted sites within right hepatic lobe (**Figure 1**). Ice balls were seen as sharp-edged, teardrop-shaped regions of signal loss on fast spin-echo MRI imaging. Ice balls demonstrated via intraprocedural MRI scans were clearly distinguishable from normal hepatic tissue (**Figure 2**). Each cryoprobe insertion site served as central axis of measurement, recording minimal and maximal ice ball diameters of 19.4 ± 1.5 mm and 44.3 ± 1.8 mm, respectively. Mean ice ball volume was 8.32 ± 2.41 cm^3.

Follow-up MRI observations

Cryolesions were readily detectable on postablation Days 2 and 7, but none were apparent in MRI studies of Days 15 and 30. All cryolesions were teardrop-shaped regions of low signal intensity on T1W images and high signal intensity on T2W images. The borders were smooth and well-defined. After cryoablation, mean cryolesion volumes on T1W and T2W images totaled 4.48 ± 1.9 cm^3 and 14.16 ± 4.1 cm^3, respectively on Day 2, compared with 3.89 ±

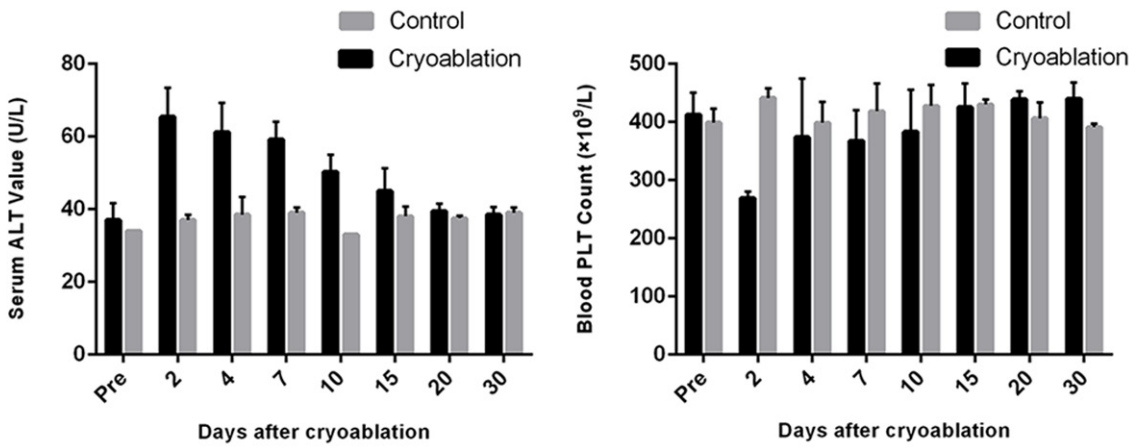

Figure 3. Mean platelet (PLT) count and alanine aminotransferase (ALT) values plotted at various test intervals in cryoablated and control animals.

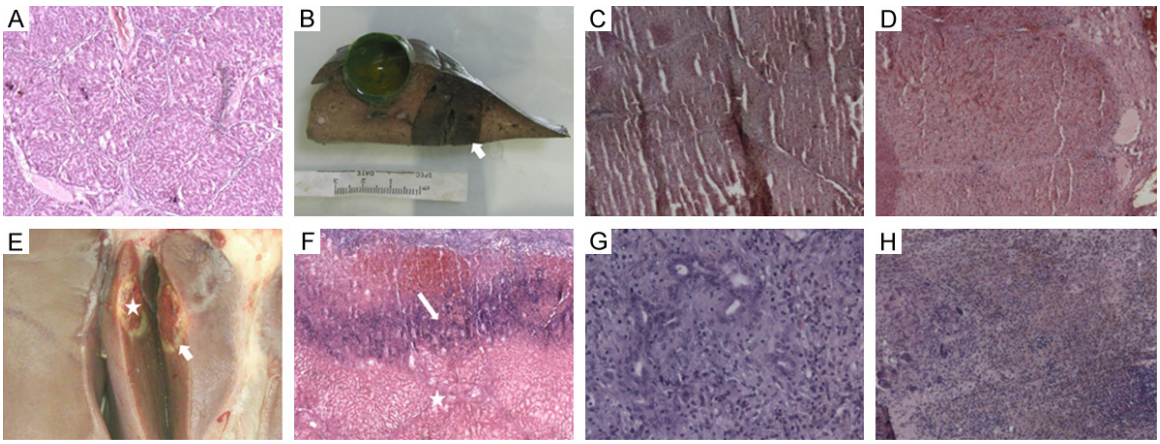

Figure 4. Pathologic features of hepatic cryolesions at various time points: A: (H&E × 30) Normal liver of control group; B: Gross specimen immediately postablation, with cryolesion presenting as dark red, elliptical zone; C: (H&E × 30) Center of cryolesion immediately postablation. Note cellular homogeneity, necrotic cells in trabecular pattern, and lobular arrangement; D: (H&E × 30) Substantial sinusoidal hemorrhage at cryolesion edge immediately postablation; E: Deep-red oval lesion (star) rimmed by thinly layered white tissue (arrow) 7 days postablation; F: (H&E × 30) Extensive central coagulative necrosis (star) 7 days postablation. Intense inflammation identified at white rim (arrow); G: (H&E × 150) Inflammation and granulation tissue at rim 7 days postablation; H: (H&E × 30) Lesion appears small and scar-like 15 days postablation, with many fibroblasts and inflammatory cells and heavy hemosiderin deposition. H&E, hematoxylin and eosin.

2.1 cm^3 and 6.45 ± 2.3 cm^3, respectively on Day 7 (**Figure 2**).

Blood test results

Mean serum ALT values of test (group 1) and control (groups 2) animals differed significantly, increasing significantly 2 days after cryoablation but returning to normal range 20 days after the procedure (**Figure 3**). Cryoablation ($P < 0.05$) and days after cryoablation ($P < 0.05$) were significant indicators of ALT level on univariate analysis. A significant association between cryoablation and days after cryoablation was also identified ($P < 0.05$). There was a significant decline in PLT count 2 days after cryoablation (**Figure 3**). Neither cryoablation nor days after cryoablation significantly impacted PLT count (both, $P > 0.05$); but cryoablation displayed a significant association with days after cryoablation ($P < 0.05$). Bilirubin, ALKP, myoglobin, creatinine, WBC count, and hematocrit values did not differ significantly by group.

Pathologic findings

In liver sampled immediately after cryoablation, cryolesions appeared as dark red, elliptical zones, corresponding well with ice ball size/shape depicted by MRI. Internally, each harbored a homogeneous mass of necrotic cells, their ghost-like remnants retaining trabecular pattern and lobular arrangement. Distinct cellular details were lost, the few nuclei present showing pyknosis and karyorrhexis. At peripheries of lesions, substantial sinusoidal hemorrhage was evident (**Figure 4**).

Minimal and maximal diameters of necrotic areas were 9.4 ± 0.8 mm and 31.2 ± 1.2 mm, respectively. The mean volume of necrotic areas (4.24 ± 2.3 cm^3) was significantly less than that of ice balls observed in MRI studies (8.32 ± 2.41 cm^3, $P < 0.05$), although MRI-determined cell necrosis isotherms were within 6.0 ± 0.8 mm of ice ball confines.

Seven days after cryoablation, lesions were deep-red oval zones (mean volume, 3.12 ± 1.8 cm^3) rimmed by thinly layered white tissue and characterized by extensive coagulative necrosis. Likewise, there was structural disintegration, leaving dilated sinusoids and shrinking hepatocytes. The white pseudocapsular rim was marked by intense inflammatory cell infiltrates and exuberant granulation tissue formation.

Fifteen days after cryoablation, the retracted lesions had developed scar-like qualities. Many fibroblasts and inflammatory cells were present, and hemosiderin was abundant. By Day 30, however, ablated areas had completely resolved.

Discussion

This study has shown that combined MRI and OSNS guidance of percutaneous liver cryoablation is effective and safe in a pig model. Through this approach, MRI monitoring ensured accurate insertion of cryoprobes into right hepatic lobes of test animals. Transition zones between frozen and non-frozen tissue were clearly visualized, confirming tissue necrosis in cryoablated areas by histologic means. Although the volume of necrotic tissue determined through pathologic assessment was less than that of ice balls gauged by MRI (4.24 ± 2.3 cm^3 vs. 8.32 ± 2.41 cm^3), cell necrosis isotherms were within 6.0 ± 0.8 mm of ice ball confines in MRI views. Follow-up MRI studies, blood tests, and pathologic examinations further underscored the efficacy and safety of this particular technique.

The merit of combining MRI and navigation technology for interventional purposes has been demonstrated by others [19-22]. The OSNS proved quite helpful in needle guidance, allowing accurate cryoprobe placement. The needle holder could be moved freely about in the open-configuration MRI system, permitting the operator to safely perform probe puncture at various sites and angles. The linear graphic overlay was exact and beneficial throughout monitoring and guidance. Hepatic respiratory movement caused no major problem during positioning of the probes. Of note, experience in percutaneous interventions is essential for time-efficient utilization.

Given the markedly reduced T2 relaxation time of ice, cryotherapy is an ideal modality for MRI monitoring [23, 24], whether T1W or T2W sequences are applied. The cryoablated areas are regularly represented as signal-void zones [18].

Early MRI visualization of ice ball formation is a clinical asset, because the cytotoxic isotherm (ie, -20 to -40°C, depending on cell sensitivity) is generally 5-10 mm behind is leading edge, so imaging allows intraoperative monitoring of the frozen zone [25-27]. Characteristic pathologic changes at 7 days postablation include the encircling of necrotic tissue by numerous fibroblasts and inflammatory cells. Prior investigations have shown that cryoablation incites a much broader inflammatory band than do hyperthermal ablation techniques. This phenomenon may result from intracellular antigen release in the aftermath of freezing [28].

In terms of safety, all animals survived and completed the entire cryoablation protocol with little consequence. Serum ALT concentrations and blood platelet counts showed transient postablative adverse changes, as seen in previous studies [29-31]. Thrombocytopenia is characteristic of cryoablation, local trapping of platelets in cryolesions being the primary cause [29].

This study has two major limitations. First, the use of a normal porcine liver model is open to criticism, owing to somewhat limited clinical applicability. However, there is currently no large-animal model of liver tumors that is perfectly suited for use with human cryoablation probes. As another issue, relatively few animals were studied.

In conclusion, open-configuration MRI and an OSNS used together in guidance of percutaneous liver cryoablation proved effective and safe in this animal model, perhaps providing an ideal means of precision hepatic ablation in clinical practice.

Disclosure of conflict of interest

None.

Address correspondence to: Jie Pan and Zhengyu Jin, Department of Radiology, Peking Union Medical College Hosptial, Chinese Academy of Medical Sciences, Shuaifuyuan 1#, Dongcheng District, Beijing 100730, China. Tel: +8610 69159562; Fax: +8610 69155441; E-mail: markpan6885@sina.com (JP); Tel: +8610 69155441; Fax: +8610 69155441; E-mail: jin_zhengyu@163.com (ZYJ)

References

[1] Ferlay J, Shin HR, Bray F, Forman D, Mathers C and Parkin DM. Estimates of worldwide burden of cancer in 2008: GLOBOCAN 2008. Int J Cancer 2010; 127: 2893-2917.

[2] European Association for the Study of the Liver; European Organisation for Research and Treatment of Cancer. EASL-EORTC clinical practice guidelines: management of hepatocellular carcinoma. J Hepatol 2012; 56: 908-943.

[3] McCarter MD and Fong Y. Metastatic liver tumors. Semin Surg Oncol 2000; 19: 177-188.

[4] Cha C, DeMatteo RP and Blumgart LH. Surgery and ablative therapy for hepatocellular carcinoma. J Clin Gastroenterol 2002; 35: S130-137.

[5] Nagorney DM and Gigot JF. Primary epithelial hepatic malignancies: etiology, epidemiology, and outcome after subtotal and total hepatic resection. Surg Oncol Clin N Am 1996; 5: 283-300.

[6] Ahmed M, Brace CL, Lee FT Jr and Goldberg SN. Principles of and advances in percutaneous ablation. Radiology 2011; 258: 351-369.

[7] Aghayev A and Tatli S. The use of cryoablation in treating liver tumors. Expert Rev Med Devices 2014; 11: 41-52.

[8] Livraghi T, Solbiati L, Meloni MF, Gazelle GS, Halpern EF and Goldberg SN. Treatment of focal liver tumors with percutaneous radio-frequency ablation: complications encountered in a multicenter study. Radiology 2003; 226: 441-451.

[9] Mazzanti R, Arena U, Pantaleo P, Antonuzzo L, Cipriani G, Neri B, Giordano C, Lanini F, Marchetti S and Gentilini P. Survival and prognostic factors in patients with hepatocellular carcinoma treated by percutaneous ethanol injection: a 10-year experience. Can J Gastroenterol 2004; 18: 611-618.

[10] Solbiati L, Livraghi T, Goldberg SN, Ierace T, Meloni F, Dellanoce M, Cova L, Halpern EF and Gazelle GS. Percutaneous radio-frequency ablation of hepatic metastases from colorectal cancer: long-term results in 117 patients. Radiology 2001; 221: 159-166.

[11] Erinjeri JP and Clark TW. Cryoablation: mechanism of action and devices. J Vasc Interv Radiol 2010; 21: S187-191.

[12] Allaf ME, Varkarakis IM, Bhayani SB, Inagaki T, Kavoussi LR and Solomon SB. Pain control requirements for percutaneous ablation of renal tumors: cryoablation versus radiofrequency ablation--initial observations. Radiology 2005; 237: 366-370.

[13] Lee SM, Won JY, Lee DY, Lee KH, Lee KS, Paik YH and Kim JK. Percutaneous cryoablation of small hepatocellular carcinomas using a 17-gauge ultrathin probe. Clin Radiol 2011; 66: 752-759.

[14] Mala T, Edwin B, Samset E, Gladhaug I, Hol PK, Fosse E, Mathisen O, Bergan A and Soreide O. Magnetic-resonance-guided percutaneous cryoablation of hepatic tumours. Eur J Surg 2001; 167: 610-617.

[15] Seifert JK, Junginger T and Morris DL. A collective review of the world literature on hepatic cryotherapy. J R Coll Surg Edinb 1998; 43: 141-154.

[16] Lam CM, Shimi SM and Cuschieri A. Ultrasonographic characterization of hepatic cryolesions. An ex vivo study. Arch Surg 1995; 130: 1068-1072.

[17] Shock SA, Laeseke PF, Sampson LA, Lewis WD, Winter TC 3rd, Fine JP and Lee FT Jr. Hepatic hemorrhage caused by percutaneous tumor ablation: radiofrequency ablation versus cryoablation in a porcine model. Radiology 2005; 236: 125-131.

[18] Silverman SG, Tuncali K, Adams DF, vanSonnenberg E, Zou KH, Kacher DF, Morrison PR and Jolesz FA. MR imaging-guided percutaneous cryotherapy of liver tumors: initial experience. Radiology 2000; 217: 657-664.

[19] Cai K, Yang R, Lin Q and Wang Z. Tracking multiple surgical instruments in a near-infrared

optical system. Comput Assist Surg (Abingdon) 2016; 21: 46-55.
[20] Lu Y, Li C, Liu M, Fritz J, Carrino JA, Wu L and Zhao B. MRI-guided stereotactic aspiration of brain abscesses by use of an optical tracking navigation system. Acta Radiol 2014; 55: 121-128.
[21] Soh E, Bearcroft PW, Graves MJ, Black R and Lomas DJ. MR-guided direct arthrography of the glenohumeral joint. Clin Radiol 2008; 63: 1336-1341; discussion 1342-1333.
[22] Blanco RT, Ojala R, Kariniemi J, Perala J, Niinimaki J and Tervonen O. Interventional and intraoperative MRI at low field scanner--a review. Eur J Radiol 2005; 56: 130-142.
[23] Tacke J, Speetzen R, Heschel I, Hunter DW, Rau G and Gunther RW. Imaging of interstitial cryotherapy--an in vitro comparison of ultrasound, computed tomography, and magnetic resonance imaging. Cryobiology 1999; 38: 250-259.
[24] Tacke J, Adam G, Haage P, Sellhaus B, Grosskortenhaus S and Gunther RW. MR-guided percutaneous cryotherapy of the liver: in vivo evaluation with histologic correlation in an animal model. J Magn Reson Imaging 2001; 13: 50-56.
[25] Littrup PJ, Jallad B, Vorugu V, Littrup G, Currier B, George M and Herring D. Lethal isotherms of cryoablation in a phantom study: effects of heat load, probe size, and number. J Vasc Interv Radiol 2009; 20: 1343-1351.
[26] Popken F, Seifert JK, Engelmann R, Dutkowski P, Nassir F and Junginger T. Comparison of iceball diameter and temperature distribution achieved with 3-mm accuprobe cryoprobes in porcine and human liver tissue and human colorectal liver metastases in vitro. Cryobiology 2000; 40: 302-310.
[27] Seifert JK, Gerharz CD, Mattes F, Nassir F, Fachinger K, Beil C and Junginger T. A pig model of hepatic cryotherapy. In vivo temperature distribution during freezing and histopathological changes. Cryobiology 2003; 47: 214-226.
[28] Ng KK, Lam CM, Poon RT, Shek TW, To JY, Wo YH, Ho DW and Fan ST. Comparison of systemic responses of radiofrequency ablation, cryotherapy, and surgical resection in a porcine liver model. Ann Surg Oncol 2004; 11: 650-657.
[29] Pistorius GA, Alexander C, Krisch CM, Feifel G, Schilling MK and Menger MD. Local platelet trapping as the cause of thrombocytopenia after hepatic cryotherapy. World J Surg 2005; 29: 657-660; discussion 661.
[30] Cozzi PJ, Stewart GJ and Morris DL. Thrombocytopenia after hepatic cryotherapy for colorectal metastases: correlates with hepatocellular injury. World J Surg 1994; 18: 774-776; discussion 777.
[31] Nair RT, Silverman SG, Tuncali K, Obuchowski NA, van Sonnenberg E and Shankar S. Biochemical and hematologic alterations following percutaneous cryoablation of liver tumors: experience in 48 procedures. Radiology 2008; 248: 303-311.